Theor Chem Acc (2006) 116: 148–159
DOI 10.1007/s00214-005-0035-7

REGULAR ARTICLE

Leticia González · Jürgen Full

A first principles approach to optimal control

Received: 6 April 2005 / Accepted: 26 October 2005 / Published online: 2 December 2005

Abstract This article shows that by using ab initio or first principle calculations it is possible to obtain reliable ingredients needed to simulate pump-probe and optimal control experiments. Our experimental challenge is to elucidate the reaction mechanism behind an optimal pulse tailored to maximize ionization in the system $CpMn(CO)_3$, while avoiding CO dissociation. Starting from MRCI/CASSCF potential energy curves calculated along the relevant CO fragmentation channel, we use the resulting MRCI wave function to estimate non-adiabatic couplings, as well as neutral-to-neutral and neutral-to-ionic dipole couplings. The state-of-the-art potentials and couplings serve to perform wave packet propagations which simulate the femtosecond pump-probe spectra that explain the features shown in the experimental optimal pulse.

Keywords Organometallics · Multiconfigurational methods · Reaction dynamics · Femtochemistry · Optimal control

1 Introduction

Quantum control of chemical reactions is a field which has awaked in the last decade, spurred by the availability of femtosecond (fs) lasers [1]. Reasons to follow up this emerging field of modern chemistry are in plenty. Chemistry is a discipline that has been born from the necessity of transforming reactants into products with the maximum efficiency. The new concept of controlling chemical reactions implies not only the need to maximize desired products and minimize by-products, but also the synthesis of new molecular species, the design of new materials, and even the execution of chemical and biological functions. The process of realization of such goals and many more is still in its formative years but is reshaping quickly. According to the prevailing experiments and based on the available theoretical simulations, it is natural to predict that the path of quantum control will provide exciting scientific knowledge and innovative technology in the near future.

In the frame of traditional chemistry one can think of achieving thermodynamic or kinetic control. Thermodynamic control is well established to the extent that variables like temperature, pressure or concentration can influence the course of a reaction; kinetic control is also well mastered by using catalysts that can reduce the reaction barrier of the desired reactive channel. These tools, however, do not access the microscopic behavior of a chemical reaction.

With the advent of photochemistry, light emerged as a powerful tool to steer reactions. Control may be achieved by exciting the system to potential energy surfaces (PESs) where the free energy between reactants and products is different from the one given in the electronic ground state. Kinetic control can be accomplished surpassing the reaction barriers by means of appropriate photo-excitations. Unfortunately, the success of this traditional photochemistry is conditioned by the quantum mechanical temporal evolution of the system as governed by the multidimensional coupled PESs. Again, however, this conventional version of photochemistry does not access the very microscopic behavior of a chemical reaction, and consequently it is difficult to predict the outcome of a reaction, let alone control it.

When nanosecond (ns) lasers became available in the 1960s, the dream revived again. It was expected that by illuminating chemical compounds with lasers, reaction paths could be steered in a preferred way. The idea relied on tuning a laser with the vibrational frequency of a particular bond so that the targeted bond is weakened and finally broken, thereby encouraging a selected product. Unfortunately, this concept, so-called mode-selective chemistry, ran up against an unexpected difficulty: the couplings between the different degrees of freedom quickly redistribute the energy deposited in a particular bond throughout the molecule. Therefore, because the typical pulse durations were too long to avoid internal vibrational redistribution (IVR) in all but exceptional

L. González (✉) · J. Full
Institut für Chemie and Biochemie, Freie Universität Berlin,
Takustrasse 3, D-14195 Berlin, Germany
E-mail: leti@chemie.fu-berlin.de

cases, selectivity was lost. Only when the vibrational modes are nearly uncoupled control is possible. The epitomized example is HOD, which possesses fundamental OH and OD vibrational stretching frequencies separated by more than $1000\,cm^{-1}$. In this case a well tuned intense infrared (IR) ns laser pulse can selectively excite a given normal mode, leading to OH+D or O+HD dissociation [2].

Looking at the time scales of molecular processes, it is clear that the duration of the first – continuous wave (cw) – lasers was much too long to intervene in the course of a reaction. While photophysical processes like fluorescence and phosphorescence occur in the ns time scale, rotations need picoseconds (ps), and vibrations and conical intersections take place within a few fs; that is, the control over the nuclear dynamics occurring in a chemical reaction needs fs resolution. Therefore, it was necessary to wait for almost 30 years to see resurgence in the field of control of chemical reactions. Theoretically, it was soon recognized that the active manipulation of the quantum dynamics needs to exploit quantum mechanical interference effects. See for instance the seminal work of Brumer and Shapiro on coherent control [3], the *pump-dump* or *pump-control* proposals from Tannor–Kosloff–Rice [4,5], or the adiabatic strategy introduced by Bergmann et al. [6] known as *stimulated Raman adiabatic passage (STIRAP).* In the aforementioned proposals the control-knobs are the phase, the time delay or the linear chirp – that is, it is one single parameter which influence the course of a reaction. Experimentally, it was the arrival of fs lasers [1] together with rigorous tools able to meet the requirements of frequency and time shapes as imposed by the theory that has made possible a burst of control activities [7].

Despite the experimental success in the control of small chemical systems (see e.g. [1,8,9]) and the many efforts invested in multidimensional dynamical studies (see e.g. [10, 11]), in most but the simplest systems, the search for an appropriate chemical path is again hampered by the incomplete knowledge of the Hamiltonian. To overcome this limitation a specially attractive control scheme based on feedback learning algorithms was introduced by Judson and Rabitz [12]. Genetic algorithms search the best pulse shapes to prepare specific products based on fitness information, such as product yields. This method, also called *close-loop* control or simply optimal control, prepares the desired target solving the Schrödinger equation exactly in real time through solving a many-parameter problem [13]. The first experimental verification of feedback or adaptive control was done in photophysics by Wilson and coworkers [14], and later manipulating chemical reactions by the group of Gerber [15,16] and others [17–19]. While the first applications of optimal control were directed to selective bond breaking [15,17,19], it should be noted that optimal control can form new bonds [18] or modify biological functions [20].

Although pragmatic, such optimal pulses have the inconvenience that no physical information about the dynamics of the system can be straightforwardly elucidated. In non-reactive systems, this issue has been addressed in different ways. For instance, one can repeat the optimization experiments with a reduced number of parameters and compare the results [13,20] or one can let the learning algorithm find control variables [21]. Other strategies to learn about the system's dynamics incorporate spectral pressure during the optimization [22], try to extract information from the experimental data with various inversion algorithms [23–27], or include liquid crystal spatial light modulators in the optimal control theory to establish a link between experimental and theoretical optimal pulses [28].

In reactive systems, the first successful understanding of optimal control was made by our group for the optimization of ionization versus ligand fragmentation in an organometallic system, $CpMn(CO)_3$. [29]. In this case, the link between theory and experiment was achieved by the explicit calculation and analysis of the properties of the molecular system. Exemplarily, our optimal pulse was designed to maximize the yield of the parent ion $CpMn(CO)_3^+$ while hindering competing fragmentation, $CpMn(CO)_2 + CO$.

For chemical reactions, like the one studied in [29], the understanding of such experimental optimal pulses involves a careful analysis of the underlying reaction dynamics. Hence, the analysis of the quantum dynamics of a chemical reaction is the primary step to ultimately guide a quantum system to some final target state.

As will be outlined in the next section, quantum dynamical simulations using wave packet propagation requires PESs. Accurate PESs must be obtained by means of quantum mechanical methods. Ab initio or first principle quantum mechanical calculations are almost routine for medium size molecules in the ground state. Most of the laser induced simulations, however, occur in electronic excited states; this is not surprising if one accounts for the fact that ultraviolet (UV) laser techniques are much better developed than IR ones. As a consequence, most of the control experiments performed in the past decades involve electronically excited states [30]. It is worth mentioning, however, that in the very last few years IR laser pulses have been being developed at good pace; see for instance [31,32], allowing the control of reactions in the electronic ground state. In any case, for theoreticians, a spectroscopic experiment in the visible–UV range means that the analysis of quantum dynamics in the electronic excited state is directly linked not only with the fascinating problem of understanding photochemical processes [33], but also with the challenging task of obtaining PESs and related molecular properties in electronically excited states.

It is the goal of this paper to show in a step-wise manner the theoretical ingredients that are needed to simulate control experiments. Since all of them are obtained starting from an ab initio wave function, we call it a *first principles* approach. The system we employ, $CpMn(CO)_3$, (where $Cp = \eta^5 - C_5H_5$), is big enough to be a representative example of a multidimensional object, but small enough to be treated in an accurate way. It is encouraging that, despite the multidimensionality of the system, a wise selection of the relevant degrees of freedom, together with accurate ab initio calculations can help to uncover the dynamical effects induced by fs optimal laser pulses.

Section 2 will present the model system and Sect. 3 will go through the first principles strategy. Section 4 will show an application of the data obtained in Sect. 3, and finally, Sect. 5 ends with a summary and an outlook.

2 Model

$CpMn(CO)_3$ is shown in Fig. 1, together with the coordinate system that is used here. Organometallic compounds containing metal and carbonyl chromophores have been the object of profound interest because fragmentation occurs in electronically excited states. A large number of studies have concentrated on pump-probe experiments that follow the dynamics of molecules electronically excited (see e.g. [34–36]). This has, of course, also prompted numerous theoretical studies (a few examples can be found in [37–42]) aiming at shedding some light on the dynamics of the ultrafast photodissociation.

The principle of the pump–probe experiments is the following: an ultrashort laser pulse – the pump – excites the molecule from the vibrational ground state of the electronic ground state to some electronically excited state, which can be bound, dissociative, or even more interesting, pre-dissociative. In any case, the system evolves in time, it can show molecular vibrations in the bond states or fragmentate in the dissociative states. Such dynamical behavior can be monitored by multi-photon ionization with a probe pulse that arrives after a well-defined time delay, interrogating the system at a particular location. Interestingly, since the detection of the products is done after ionization, the path the system follows after excitation is not a trivial question. Indeed, fragmentation may occur either on neutral or on ionic surfaces without any difference in the detected fragmented ions. This dilemma has recently received a great deal of attention. For instance, Trushin et al. [43] have studied dissociative ionization of different metal carbonyls, $Ni(CO)_4$, $Fe(CO)_5$ and $Cr(CO)_6$ at intensities between 10^{12}–$10^{14}\,W\,cm^{-2}$ finding that neutral dissociation can be practically neglected; fragmentation is instead rationalized by resonances in ions. On the other hand, our simulations indicate that the photodissociation of $CpMn(CO)_3$ [29] starts on neutral surfaces.

Additionally, since carbonyl systems have interesting dynamics, they were the first candidates to be used in optimal control experiments; see the pioneer work of Gerber and coworkers [15] on $CpClFe(CO)_2$.

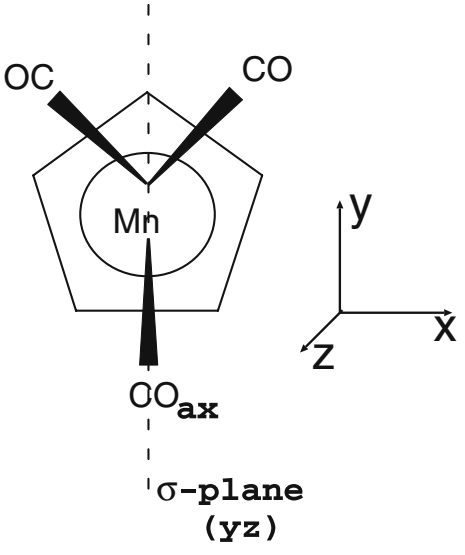

Fig. 1 View of $CpMn(CO)_3$ from the top, together with the coordinate system used in the calculation of the potential energy surfaces (adapted from [45]). CO_{ax} stands for the axial carbonyl that is dissociated

3 A first principles procedure

In this section, we will explain the procedure to simulate the dynamics underlying optimal pulses. The time evolution of a system is simulated by laser driven nuclear wave packets $|\Psi(t)>$ calculated as solution of the time-dependent Schrödinger equation,

$$i\hbar\frac{\partial}{\partial t}|\Psi(t)\rangle = \hat{H}(t)|\Psi(t)\rangle. \tag{1}$$

In the total Hamiltonian operator of the system $\hat{H}(t)$,

$$\hat{H}(t) = \hat{T} + \hat{V} + \hat{W}(t). \tag{2}$$

$\hat{T}$ is the kinetic operator of the nuclei and $\hat{V}$ the electronic potential, which is calculated from the time-independent Schrödinger equation within the Born–Oppenheimer frame using ab initio methods, see Sect. 3.1. Both parts form the molecular Hamiltonian, while $\hat{W}(t)$ is the time-dependent interaction of the molecule with an electromagnetic field, a laser pulse in our case.

Because we propagate on more than one electronic state, the wave function $|\Psi(t)>$ is more conveniently written as a vector and the Hamiltonian operator as a matrix. Eq. (1) then becomes,

$$i\hbar\frac{\partial}{\partial t}\begin{pmatrix}|\Psi^0(t)\rangle\\ \vdots\\ |\Psi^n(t)\rangle\end{pmatrix} = \begin{pmatrix}\hat{H}_{0,0} & \dots & \hat{H}_{0,n}\\ \vdots & \ddots & \vdots\\ \hat{H}_{n,0} & \dots & \hat{H}_{n,n}\end{pmatrix}\begin{pmatrix}|\Psi^0(t)\rangle\\ \vdots\\ |\Psi^n(t)\rangle\end{pmatrix} \tag{3}$$

wherein the indexes $0, 1, \dots, n$ denote the involved (neutral and ionic) electronic states.

In the adiabatic representation, the matrix elements $\hat{H}_{jk}$ of the Hamiltonian are composed of the following terms:

$$\hat{H}_{jk} = \delta_{jk}\,(\hat{T} + V_j) - \frac{\hbar^2}{2\,m}\,(\,T^{(2)}_{jk} + 2T^{(1)}_{jk}\nabla\,)\,. \tag{4}$$

The kinetic or non-adiabatic couplings between the electronic states j and k, $T^{(1)}_{jk}$ and $T^{(2)}_{jk}$ are defined as

$$T^{(1)}_{jk}(Q) = \left\langle \Phi_j(Q) \,\middle|\, \frac{\partial}{\partial Q}\,\Phi_k(Q)\right\rangle \tag{5a}$$

$$T^{(2)}_{jk}(Q) = \left\langle \Phi_j(Q) \,\middle|\, \frac{\partial^2}{\partial Q^2}\,\Phi_k(Q)\right\rangle, \tag{5b}$$

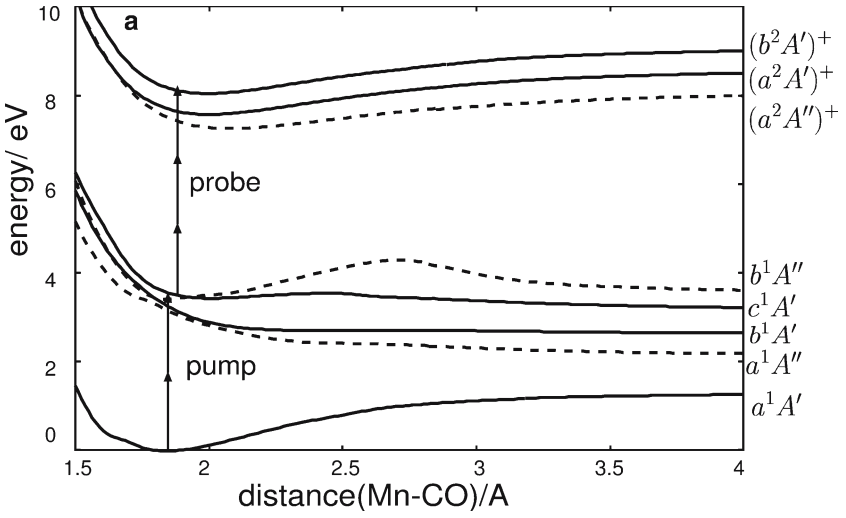

Fig. 2 Adiabatic neutral and ionic MRCI/CASSCF potential energy curves as a function of the Mn–CO elongation. *Solid lines* stand for states of A' symmetry and *dashed lines* for states of A'' symmetry, in the C_s point group. *Arrows* indicate which states are populated after the multiphoton pump and probe pulse, respectively

where $\Phi_j(Q)$ are the time-independent electronic wave functions and Q represents the nuclear degrees of freedom considered in the problem.

The operator for the interaction of the molecule with the laser field $\hat{W}(t)$, as used in Eq. (2), is described by the semiclassical dipole approximation,

$$\hat{W}(t) = -\boldsymbol{\mu}_{ij} \cdot \mathbf{E}(t), \tag{6}$$

where $\boldsymbol{\mu}_{ij}$ is the transition dipole moment between molecular or ion electronic states i and j ($\boldsymbol{\mu}_{ii}$ describes the permanent dipole moment for the state i), and $\mathbf{E}$ the time-dependent electric laser field. The laser field $\mathbf{E}(t)$ used in these simulations is given by the following expression:

$$\mathbf{E}(t) = \mathbf{e}E^0 \cos(\omega t) \cdot s(t), \tag{7}$$

where $\mathbf{e}$ is the polarization direction of the field, E^0 is the amplitude of the field, ω the carrier frequency and $s(t)$ the shape function

$$s(t) = \sin^2\left(\frac{\pi(t - t_\mathrm{d})}{t_\mathrm{p}}\right) \qquad \text{for} \quad t_\mathrm{d} \le t \le t_\mathrm{d} + t_\mathrm{p}, \tag{8}$$

with t_p being the pulse duration and t_d the time delay.

In summary, the decoding of the optimal pulse requires an analysis of the dynamical processes that take place under irradiation (cf. Eq. (1)), in this case a pump-probe process, but to solve for the Hamiltonian, we need first reliable PESs (cf. Eq. (2)) which can be obtained with the help of ab initio methods.

In general, when looking at Eqs. (4) and (6), it is obvious that the solution of Eq. (3) requires the following functions: (a) a set of PESs described by ab initio methods, which provide reliable wave functions for the electronic (neutral and ionic) states involved in the problem, (b) the non-adiabatic couplings between electronic excited states, and (c) the dipole couplings with the laser, those involving the transition from the ground to excited neutral states as well as those relating the excited neutral states to the ionic states.

Our analysis therefore starts with a review of the low-lying excited states of $CpMn(CO)_3$, and it will be explained later on how to obtain the different couplings (b) and (c) starting from the ab initio wave function.

3.1 Potential energy surfaces

The electronic excited states of $CpMn(CO)_3$ and PESs along the relevant Mn–CO coordinate can be found in [44] and [45]. Here we present just a short summary of the involved configurations in order to understand the following subsections.

Because we are dealing with a CO fragmentation, the potential energy curves (PECs) have been computed assuming that the C_S symmetry is retained along the reaction path corresponding to the loss of the axial CO (see Fig. 1). This assumption is justified in view of the time-scale of the primary photoprocess investigated, namely the CO loss which occurs within a few tens of fs [29,46]. The relevant one-dimensional neutral and ionic PECs, V(Q), (with Q = [Mn–CO]) are shown in Fig. 2. Calculations have been obtained through state-averaged CASSCF calculations supplemented by a multireference configuration interaction (MRCI) treatment [44, 45]. The low-lying ionic states have been calculated as single roots at the MRCI/CASSCF level of theory.

The a^1A' electronic ground state conforms to a close shell electronic configuration of $(20a')^2(21a')^2(22a')^2(12a'')^2$ (13 $a'')^2$ assigned to $(2\pi_{Cp})^2(3d_{z^2})^2(3d_{x^2-y^2})^2(3\pi_{Cp})^2(3d_{xy})^2$. The low-lying virtual orbitals correspond to $3d_{yz}(23a')$, $3d_{xz}$ $(14a'')$ and $\pi^*_{CO}(24a', 25a', 15a''$ and $16a'')$.

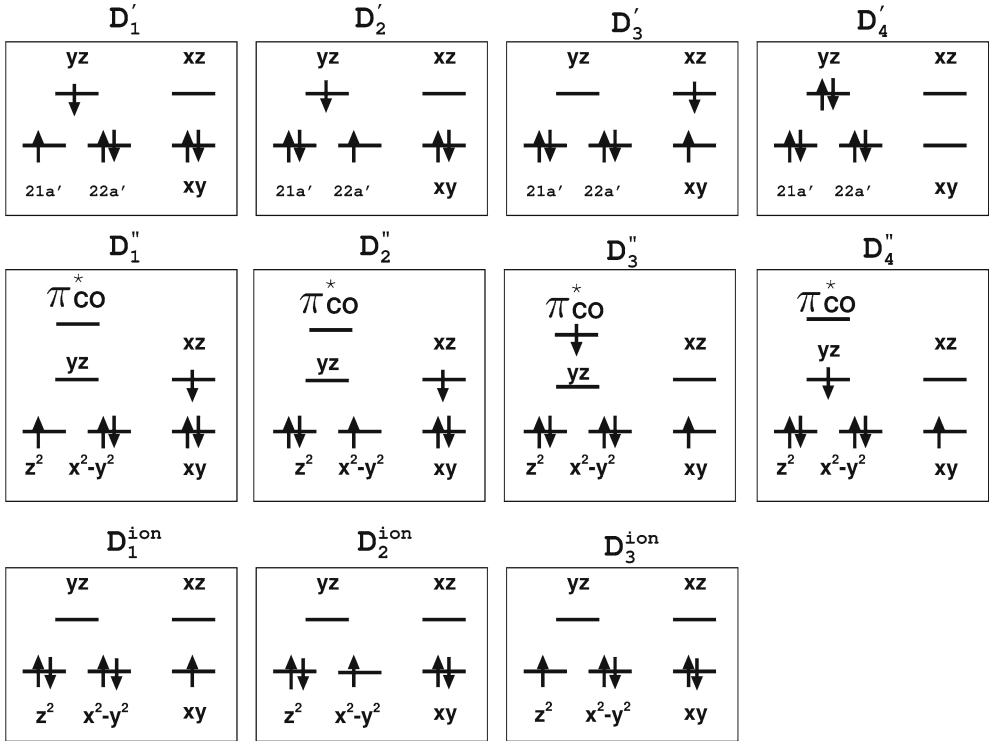

Fig. 3 Occupation schemes of the main Slater determinants that contribute to the neutral singlet excited states of $^1A'$ (D'_i) and $^1A''$ symmetry (D''_i), and to the ionic doublet states $^2A'$ and $^2A''$ (D^{ion}_i)

The electronic states can be described as a linear combination of different state configurations or Slater determinants, i.e., configuration interaction (CI)

$$|\Phi_v(Q)\rangle = \sum_j C_{vj}(Q)|D_j(Q)\rangle, \tag{9}$$

where the $|D_j(Q)\rangle$ are the Slater determinants representing any of the neutral electronic states and C_{vj} are the corresponding CI expansion coefficients. Furthermore, in the CASSCF procedure, the orbitals are simultaneously optimized along with the CI coefficients. The determinants D_j are assumed to be real and orthonormal:

$$\langle D_j(Q)|D_k(Q)\rangle = \delta_{jk}. \tag{10}$$

Analyzing the four low-lying neutral excited states of symmetry A', one sees that they are composed of four main configurations, which we will denote by D'_1, D'_2, D'_3 and D'_4 respectively. These configurations, which are illustrated in Fig. 3, differ in the occupation of the highest occupied molecular orbitals for each symmetry. Some orbitals, i.e., $23a'$, $13a''$ and $14a''$ show a leading coefficient for one $3d$-orbital: $23a'$ is mainly a $3d_{yz}$, $13a''$ a $3d_{xy}$ and $14a''$ a $3d_{xz}$ orbital. In contrast, orbitals $21a'$ and $22a'$ are linear combinations of the $3d_{z^2}$ and $3d_{x^2-y^2}$ orbitals, that we will write as $21a' \approx k_{21,z^2} \cdot 3d_{z^2} + k_{21,x^2-y^2} \cdot 3d_{x^2-y^2}$, and $22a' \approx k_{22,z^2} \cdot d_{z^2} + k_{22,x^2-y^2} \cdot d_{x^2-y^2}$, where the coefficient $k_{i,j}$ represents the standard linear expansion of the molecular orbital into atomic orbitals.

The electronic configurations of the low-lying four excited states of symmetry A'' consist of the dominant transitions shown schematically in Fig. 3. The molecular orbitals entering in the electronic configurations are mostly pure and all excitations are $3d$–$3d$ transitions except one which is a transition to a π^*_{CO}-orbital. Because the π^*_{Cp} ($22a'$) orbital remains doubly occupied in all considered configurations, it is skipped in Fig. 3.

Likewise, the ionic states can also be described by a linear expansion of configurations:

$$|\Phi^{\text{ion}}_\lambda(Q)\rangle = \sum_l C^{\text{ion}}_{\lambda l}(Q)|D^{\text{ion}}_l(Q)\rangle, \tag{11}$$

where the $|D^{\text{ion}}_l\rangle$ are the state configurations representing the ionic state, and $C^{\text{ion}}_{\lambda l}$ are the CI expansion coefficients. However, the important three energetically lowest states, a^2A'', a^2A' and b^2A' states are each described by a pure dominant configuration that differs from the ground state by removing one electron from the $3d_{xy}$, the $3d_{x^2-y^2}$ and the $3d_{z^2}$ orbital, respectively (see Fig. 3).

3.2 Non-adiabatic couplings

The non-adiabatic or kinetic coupling terms $T^{(1)}$ and $T^{(2)}$ are given in Eqs. (5a) and (5b), respectively. Substituting Eq. (9) in Eq. (5a) leads to [47]

$$T^{(1)}_{\mu\nu}(Q) = \left\langle \sum_j C_{\mu j}(Q) D_j(Q) \left| \frac{\partial}{\partial Q} \sum_k C_{\nu k}(Q) D_k(Q) \right\rangle \right.$$
$$= \sum_j \sum_k C_{\mu j} \left(\frac{\partial}{\partial Q} C_{\nu k} \right) \langle D_j(Q) | D_k(Q) \rangle$$
$$+ \sum_j \sum_k C_{\mu j}(Q) C_{\nu k}(Q) \left\langle D_j(Q) \left| \frac{\partial}{\partial Q} D_k(Q) \right\rangle \right. \quad (12)$$

Making use of Eq. (10) and defining

$$A^{(1)}_{\mu\nu} = \sum_j C_{\mu j} \left(\frac{\partial}{\partial Q} C_{\nu j} \right) \quad (13)$$

and

$$B^{(1)}_{\mu\nu} = \sum_j \sum_k C_{\mu j}(Q) C_{\nu k}(Q) \tau_{jk}, \quad (14)$$

where τ_{jk} is given by,

$$\tau_{jk} = \left\langle D_j(Q) \left| \frac{\partial}{\partial Q} D_k(Q) \right\rangle \right. \quad (15)$$

we obtain a useful expression to calculate $T^{(1)}$ from a multi-configurational wave function [47],

$$T^{(1)}_{\mu\nu}(Q) = A^{(1)}_{\mu\nu} + B^{(1)}_{\mu\nu}. \quad (16)$$

The term $A^{(1)}_{\mu\nu}$ can be considered like the CI-term, since it involves the differentiation of the CI coefficients which enter in the Eq. (9). The second term, $B^{(1)}_{\mu\nu}$, contains the derivatives of the configurations or determinants, in other words, takes into account the change of the orbitals along the reaction coordinate; thus, it will be referred to as the MO-term.

Knowing $T^{(1)}$ the calculation of the $T^{(2)}$ is straightforward [48]:

$$\underline{\underline{T}}^{(2)} = \frac{\partial}{\partial q_a} \underline{\underline{T}}^{(1)} + \underline{\underline{T}}^{(1)} \cdot \underline{\underline{T}}^{(1)}. \quad (17)$$

In calculating the matrix elements given in τ_{jk} (cf. Eq. (15)) it is useful to remember that because $\frac{\partial}{\partial Q}$ is a one-particle operator, according to the Condon–Slater rules, matrix elements are non-zero only if the determinants D_j and D_k differ in less than two orbitals. Therefore, from the state configurations shown in Fig. 3 for the A′ state and applying the Condon–Slater rules it follows that,

$$\left\langle D'_1(Q) \left| \frac{\partial}{\partial Q} D'_4(Q) \right\rangle \right. = \left\langle D'_2(Q) \left| \frac{\partial}{\partial Q} D'_4(Q) \right\rangle \right.$$
$$= \left\langle D'_3(Q) \left| \frac{\partial}{\partial Q} D'_4(Q) \right\rangle \right.$$
$$= \left\langle D'_1(Q) \left| \frac{\partial}{\partial Q} D'_3(Q) \right\rangle \right.$$
$$= \left\langle D'_2(Q) \left| \frac{\partial}{\partial Q} D'_3(Q) \right\rangle \right. = 0\,. \quad (18)$$

and the only non-vanishing matrix elements are:

$$\left\langle D'_1(Q) \left| \frac{\partial}{\partial Q} D'_2(Q) \right\rangle \right. = - \left\langle D'_2(Q) \left| \frac{\partial}{\partial Q} D'_1(Q) \right\rangle \right., \quad (19)$$

because only D'_1 and D'_2 differ in a single excitation, while the other matrix elements involve two or more electron exchanges. These elements can be easily calculated under the assumption that the atomic orbitals are orthonormal and do not change significatively along the reaction coordinate. Recalling the composition of the molecular orbitals $21a'$ and $22a'$, it is possible to write,

$$\tau_{12} = \left\langle D'_1(Q) \left| \frac{\partial}{\partial Q} D'_2(Q) \right\rangle \right. = \left\langle 22a' \left| \frac{\partial}{\partial Q} 21a' \right\rangle \right.$$
$$= \left\langle k_{22,z^2} \cdot d_{z^2} + k_{22,x^2-y^2} \cdot d_{x^2-y^2} \right.$$
$$\left. \left| \frac{\partial}{\partial Q} \left(k_{21,z^2} \cdot d_{z^2} + k_{21,x^2-y^2} \cdot d_{x^2-y^2} \right) \right\rangle \right.$$
$$\approx k_{22,z^2} \frac{\partial}{\partial Q} k_{21,z^2} + k_{22,x^2-y^2} \frac{\partial}{\partial Q} k_{21,x^2-y^2} \quad (20)$$

and

$$\tau_{21} = \left\langle D'_2(Q) \left| \frac{\partial}{\partial Q} D'_1(Q) \right\rangle \right. = -\tau_{12} = \left\langle 21a' \left| \frac{\partial}{\partial Q} 22a' \right\rangle \right.$$
$$= \left\langle k_{21,z^2} \cdot d_{z^2} + k_{21,x^2-y^2} \cdot d_{x^2-y^2} \right.$$
$$\left. \left| \frac{\partial}{\partial Q} \left(k_{22,z^2} \cdot d_{z^2} + k_{22,x^2-y^2} \cdot d_{x^2-y^2} \right) \right\rangle \right.$$
$$\approx k_{21,z^2} \frac{\partial}{\partial Q} k_{22,z^2} + k_{21,x^2-y^2} \frac{\partial}{\partial Q} k_{22,x^2-y^2}, \quad (21)$$

where k_{ij} are the corresponding coefficients of the molecular expansion.

The averaged terms τ_{12} and τ_{21} are shown in Fig. 4, together with the calculated $A^{(1)}_{bc}$ and $A^{(1)}_{cb}$, as well as $B^{(1)}_{bc}$ and $B^{(1)}_{cb}$, terms. Using Eq. (16) we can obtain the first order kinetic coupling element $T^{(1)}_{bc}$ between the states $b^1\mathrm{A}'$ and $c^1\mathrm{A}'$, see Fig. 5a. From Eq. (17) we obtain the second order kinetic coupling $T^{(2)}_{bc}$ between the same states; this is shown in Fig. 5b. Non-adiabatic couplings between other states of A′ or A″ symmetry can be calculated in a similar fashion. As regards the relevant potentials shown in Fig. 2, it is important to mention that the coupling between the states $b^1\mathrm{A}'$ and $c^1\mathrm{A}'$ is very weak, while that between the states $a^1\mathrm{A}''$ and $b^1\mathrm{A}''$ is very strong. As a result, non-adiabatic losses are only expected to occurr between the $a^1\mathrm{A}''$ and $b^1\mathrm{A}''$ states.

3.3 Dipole couplings

The interaction with the laser is defined by the dipole couplings given in Eq. (6). In order to calculate pump-probe signals, one needs not only (a) transition dipole moments (TDM) between the ground and the electronic excited states,

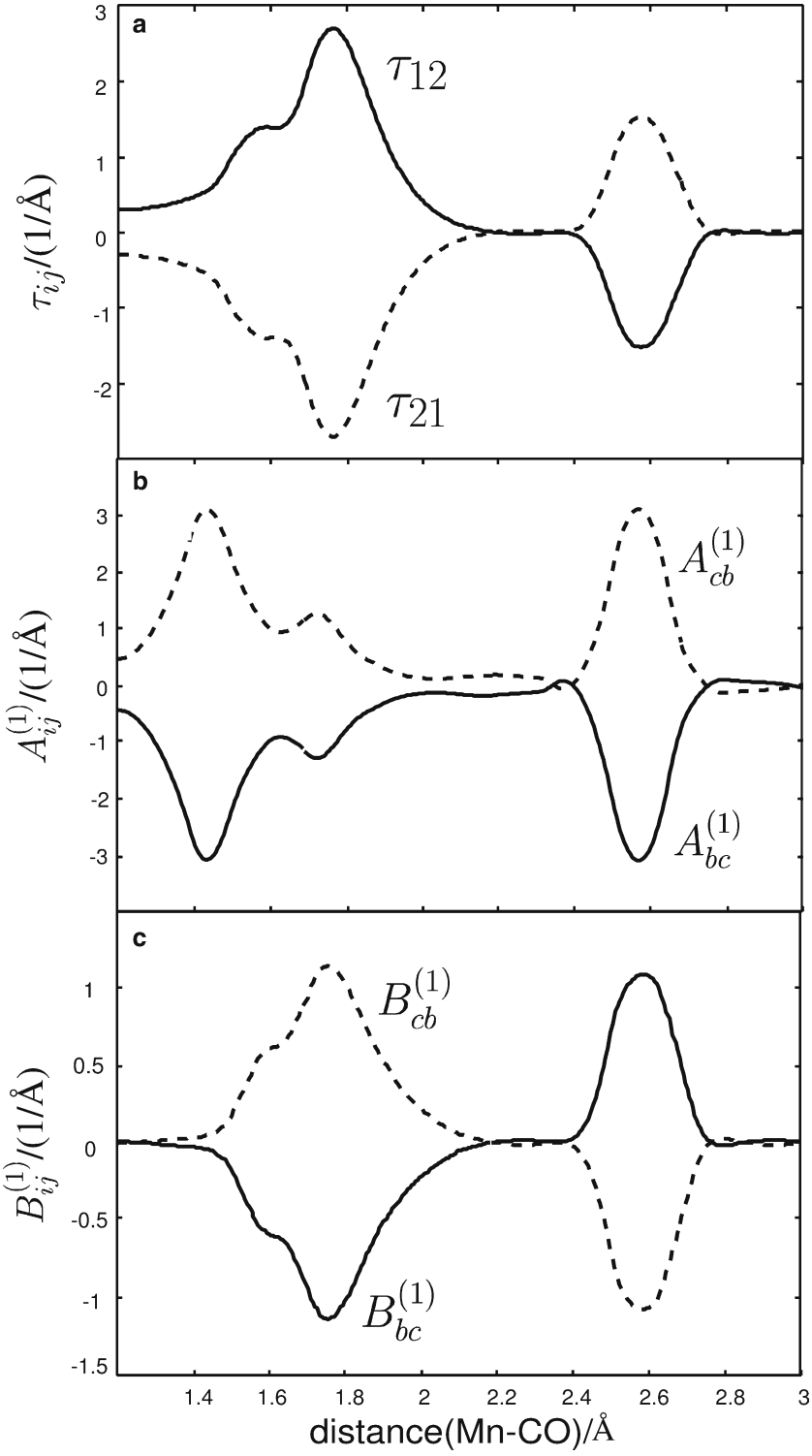

Fig. 4 Contributions to the non-adiabatic couplings between the b^1A' and c^1A' states. **a** τ_{12}, as defined in Eq. (15): **b** Elements $A^{(1)}_{bc}$ and $A^{(1)}_{cb}$, as defined in Eq. (16): **c** Elements $B^{(1)}_{bc}$ and $B^{(1)}_{cb}$, as defined in Eq. (16)

but also (b) TDM between the neutral excited states and the ionic states. In the former case, the TDM are routinely calculated at the same level of theory as the PES, i.e., in this case with the MRCI/CASSCF method. In the latest case, such calculation is by no means standard; as a consequence, it is very often that the Condon approximation is assumed, that is that the neutral-to-ionic TDM is set to a constant equal to one. In [49] however, we have suggested a procedure to

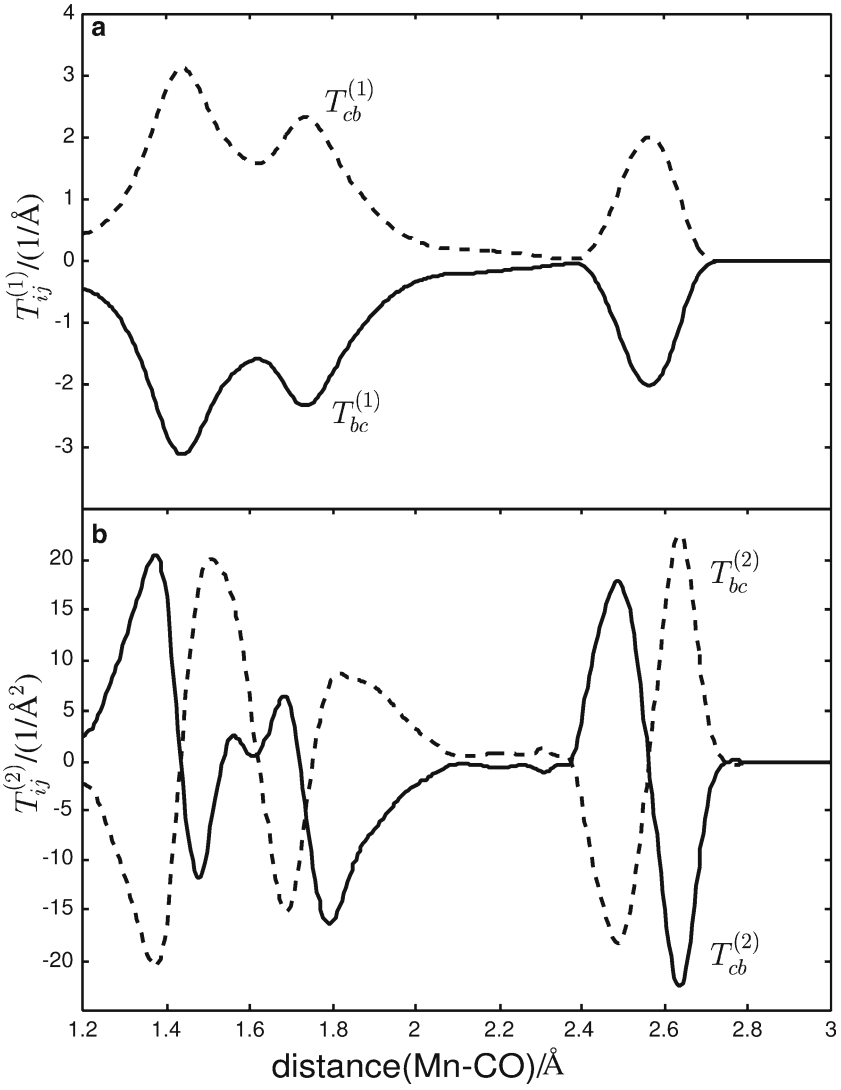

Fig. 5 Numerical non-adiabatic or kinetic coupling between the b^1A' and c^1A' states, calculated from the CI- and MO-coefficients of the multireference configuration interation (MRCI) wave function. (a) $T_{bc}^{(1)}$, (b) $T_{bc}^{(2)}$

calculate coordinate dependent neutral-to-ionic TDM starting from multiconfigurational wave functions.

Specifically, the transition dipole element for a transition from the neutral excited state Φ_ν to the ionic state $\Phi_\lambda^{\text{ion}}$ mediated by the total electronic dipole operator $\mathbf{M}$

$$\mathbf{M} = \sum_i^N \boldsymbol{\mu}_i \tag{22}$$

with N electrons can be approximately calculated as [49]

$$\langle \Phi_\nu | \mathbf{M} | \Phi_\lambda^{\text{ion}} \rangle \approx \sum_j{}' \sum_l{}' C_{\nu j} C_{\lambda l}^{\text{ion}} \cdot \det(U_\alpha) \cdot \det(U_\beta) \cdot \langle \chi_{j\nu} | \boldsymbol{\mu} | \chi_{ZEKE} \rangle \tag{23}$$

where χ_{ZEKE} is the orbital corresponding to the ionized electron, the factor $\det(U_\alpha) \cdot \det(U_\beta)$ accounts for the overlap between those orbitals with α and β spins that are not frozen during the ionization process, and $C_{\nu j}$ and $C_{\lambda l}^{\text{ion}}$ are the CI expansion coefficients defined in Eqs. (9) and (11), respectively. The prime $'$ indicates that the sum is made only over the CI-coefficients belonging to determinants that differ by one and only one spin orbital from the initial Slater determinant. This is a consequence of the Slater–Condon rules, i.e., matrix elements are zero if the two determinants involved differ by two or more spin orbitals.

In the excited states characterizing $CpMn(CO)_3$, $\det(U_\alpha) \cdot \det(U_\beta)$ is just given by $\langle \chi_m | \tilde{\chi}_m \rangle$ [49], i.e., by the overlap between the spin orbitals which relax in going from the neutral to the ionic determinant. Furthermore, the ionic states of $CpMn(CO)_3$ can be safely defined by a single configuration (see Sect. 3.1). Hence, assuming that the matrix element $\langle \chi_{j\nu} | \boldsymbol{\mu} | \chi_{ZEKE} \rangle$ is a constant, Eq. (23) reduces to

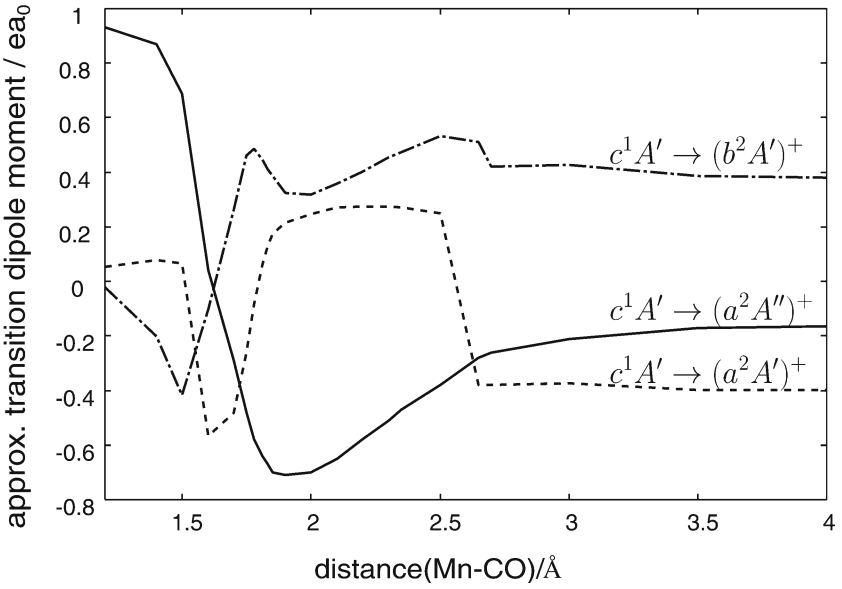

Fig. 6 Neutral-to-ionic zero kinetic energy (ZEKE) dipole couplings between the ionic states a^2A''(—), a^2A'(- - -), b^2A'(–·–) and the neutral excited state c^1A' of $CpMn(CO)_3$ (in arb. units)

$$\langle \Phi_\nu | \mathbf{M} | \Phi_\lambda^{\text{ion}} \rangle \approx \text{const.} \sum_j{}' C_{\nu j} \langle \chi_m | \tilde{\chi}_m \rangle$$
$$\approx \sum_j{}' C_{\nu j} \langle \chi_m | \tilde{\chi}_m \rangle. \quad (24)$$

Equation (24) tells us that the first step in calculating the TDM between a particular excited state and a neutral one is to identify those neutral and ionic configurations that differ in only one orbital. Then, their coordinate dependent CI-coefficients will approximately provide the coordinate dependence of the TDM. As example, let us take $\Phi_\lambda^{\text{ion}} = (a^2A'')^+$ and $\Phi_\nu = c^1A'$. Then, from Fig. 3 we see that the TDM from $c^1A' \rightarrow (a^2A'')^+$ must be proportional to the coefficient $C_{c,3}$ (where c denotes c^1A' and 3 the Slater determinant D_3'), since the ionic configuration $D_1^{\text{ion}}(a^2A'')$ differs in only one orbital, from the configuration D_3', but in more than one orbital from D_1', D_2' and D_4'. For this particular transition the rest of the orbitals remain frozen; therefore, the CI-coefficient $C_{c,3}$ is the only term entering in Eq. (24),

$$\langle c^1A' | \mathbf{M} | (a^2A'')^+ \rangle \approx C_{c,3}(Q) \quad (25)$$

To find the transition dipole moments between the c^1A' excited states and the other two ionic states, the mixing between the $3d_{x^2-y^2}$ and the $3d_{z^2}$ character present in the orbitals $21a'$ and $22a'$ has to be taken into account. Consequently, the corresponding neutral-to-ion TDM are given by [49],

$$\langle c^1A' | \mathbf{M} | (a^2A')^+ \rangle \approx C_{c,1} \langle 21' | 3d_{x^2-y^2} \rangle + C_{c,2} \langle 22' | 3d_{x^2-y^2} \rangle \quad (26)$$

and

$$\langle c^1A' | \mathbf{M} | (b^2A')^+ \rangle \approx C_{c,1} \langle 21a' | 3d_{z^2} \rangle + C_{c,2} \langle 22a' | 3d_{z^2} \rangle \quad (27)$$

The resulting transition dipole moments for the exemplary c^1A' state are plotted in Fig. 6.

4 Application

The optimal pulse obtained in [29] for the maximization of the ionization, i.e., maximum signal of the $CpMn(CO)_3^+$ peak, resulted in a pulse shape showing two main peaks of intensities 2:3. The initial wavelength used in the control experiment was of 800 nm (1.55 eV). In contrast, the optimized first subpulse was blue shifted to 798.7 nm, while the frequency of the second one was almost not changed (800.1 nm) with respect to the initial central wavelength. The initial transform-limited pulse had 87 fs of duration; the two optimized subpulses are separated by ca. 85 fs and have durations of about 40 fs.

The task now is to puzzle out how the structure of the optimal pulse controls the dynamics of the system towards the desired direction. The time profile of the pulse, together with the intensity ratio of 2:3 suggest that the initial transform-limited pulse has been divided into two subpulses designed to perform a pump-probe experiment with optimal frequencies and optimal time delays. According to the excitation energies of the neutral excited PESs (see Fig. 2), it is reasonable to assume that the first subpulse is tailored to achieve a two-photon excitation of $CpMn(CO)_3$ to any of the electronic excited states. After some optimal delay, the second subpulse excites population to an ionic state in a three-photon process. The reaction mechanism is such that predominantly the parent ion should be obtained, while CO fragmentation should be avoided. This implies that the excited states that are populated after the pump pulse must be bound or show weak non-adiabatic couplings.

In the following, we will use the PESs and couplings obtained in Sect. 3 to simulate the pump-probe spectrum which can explain the dynamics behind the optimal pulse.

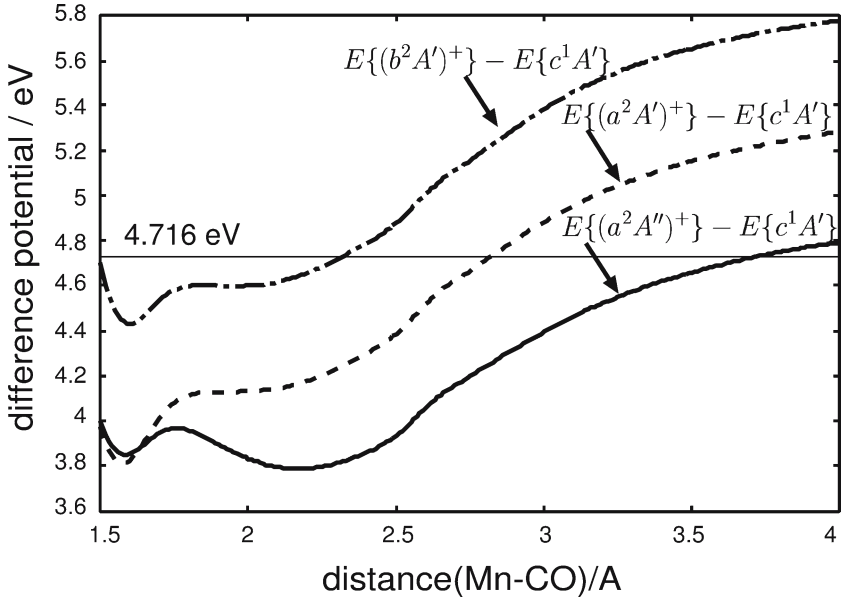

Fig. 7 Difference potentials between the ionic states a^2A''(—), a^2A'(- - -), b^2A'(–·–) and the neutral excited c^1A' state. The *horizontal line* indicate the photon energy 4.716 eV of the probe laser pulse

Inspection of the neutral adiabatic PECs depicted in Fig. 2 indicates that there exists several avoided crossings around the Franck–Condon geometry at ca. 1.8 Å [45]: one is between the b^1A' and c^1A' states and another between the a^1A'' and b^1A'' states, respectively. The adiabatic b^1A' potential is dissociative leading directly to the primary products CO + MnCp $(CO)_2$ whereas the c^1A' presents a small energy barrier around 2.5 Å that will prevent dissociation. The a^1A'' and b^1A'' states are nearly degenerate around the equilibrium geometry and avoid each other at this point; a^1A'' dissociates into CO + $MnCp(CO)_2$, whereas b^1A'' is bound. Taking into account the non-adiabatic couplings calculated in Sect. 3.2 we can predict that out of the four states that are energetically accessible within the pump pulse (cf. Fig. 2) only the c^1A' state avoids dissociation. Indeed, wave packet propagations in the b^1A'' state indicated that CO fragmentation takes place due to the strong non-adiabatic couplings with the a^1A'' state [45].

To populate the c^1A' state we employ a pump laser of 3.49 eV, equivalent to two photons of 1.745 eV each (discrepancies with the experimental laser energies are within the error of the calculated PES, typically of 0.1–0.3 eV). To probe the system we employ a probe laser of 4.716 eV, equivalent to three photons of 1.572 eV. To see which ionic states (cf. Fig. 2) are accessed with this energy we plot the difference potentials between the c^1A' state and the three lowest ionic potentials. In Fig. 7 we see that the probe pulse is resonant to the $(b^2A')^+$ state at 2.3 Å; this nuclear configuration is located slightly before the barrier maximum of the c^1A' neutral excited state. 4.716 eV is also resonant with the other two ionic states, $(a^2A')^+$ and $(a^2A'')^+$, at values larger than 2.5 Å. After exciting to the c^1A' state a big part of the wave packet is trapped in the potential well. Therefore, the wave packet cannot be probed to the energetically lower ionic states, $(a^2A')^+$ and $(a^2A'')^+$, because these states are resonant only after the barrier. Moreover, the TDM corresponding to the $c^1A' \rightarrow (b^2A')^+$ transition (Fig. 6) is larger than that corresponding value for the transitions to other ionic states. As a result, we can conclude that contributions from the a^2A'' and b^2A'' ions are negligible and the only ionic state that contributes to the pump-probe signal is the energetically highest ionic state, $(b^2A'')^+$.

The resulting pump-probe spectrum is shown in Fig. 8. According to the pump frequency, the main part of the wave packet is trapped in the c^1A' potential, but it releases population each time it reaches the barrier centered around 2.3 Å [45]. The resulting slowly decaying signal shows maxima at 85 and 260 fs and minima at 180 and 360 fs. Obviously it is most efficient to probe the system before population decays. Thus, after 85 fs (first maximum), shortly before the barrier, when the wave packet has reached 2.5 Å the second subpulse prepares the parent ion in the $(b^2A'')^+$ state.

5 Summary and outlook

An optimal control pulse tailored to enhance ionization while avoiding CO fragmentation in the organometallic complex $CpMn(CO)_3$ has been studied. Using accurate ab initio or first principles calculations and wave packet simulations we have interpreted the reaction dynamics induced by the optimal field.

First, ab initio MRCI/CASSCF potential energy curves have been calculated for the low-lying neutral singlet and doublet ionic states along the Mn-CO coordinate of $CpMn(CO)_3$. Triplet states are not considered since the loss

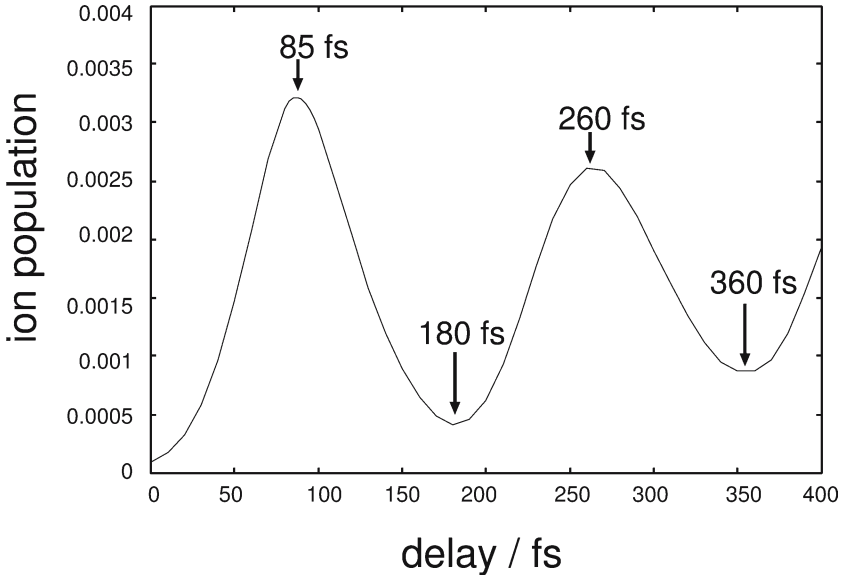

Fig. 8 Pump-probe spectrum of $CpMn(CO)_3$ obtained using a pump laser of 3.49 eV and a probe laser of 4.716 eV

of the first CO takes place in less than 200 fs. Next, non-adiabatic couplings have been approximately calculated using the leading CI and MO coefficients of the MRCI wave function. With the experimental photon energies, only the lowest neutral excited singlet states, b^1A', c^1A', a^1A'' and b^1A'' can be populated. These neutral excited states, the electronic ground state a^1A', and the ionic doublet states $(a^2A'')^+$, $(a^2A')^+$ and $(b^2A')^+$ have been included in our theoretical simulations of the pump-probe and control experiments. Finally, ab initio transition dipole moments for transitions betweeen the ground and the excited electronic states have been calculated at the MRCI/CASSCF level of theory, and transition dipole moments between excited neutral to the ionic states have been estimated using the CI and MO coefficients of the MRCI wave function.

Using the former *first principles* information our wave packet propagations in the adiabatic representation indicate that the mechanism to optimize the parent ion yield must avoid population on the b^1A'' and b^1A' states and instead it should predominantly excite the bound c^1A' state. The probe pulse should be resonant to an ionic state at a nuclear configuration previous to the c^1A' potential barrier, otherwise population would decay by dissociation into neutral fragments. According to the difference potentials and the intensity of the neutral-to-ionic transition dipole moments it is only the $(b^2A')^+$ state which fulfill these requirements. The theoretical pump-and-probe spectrum which populates the c^1A' and the $(b^2A')^+$ states, respectively, indeed predicts that the experimental delay between the two subpulses corresponds to an optimal delay time of 85 fs between the pump and the probe pulse.

In summary, this work demonstrates that based on accurate ab initio or first principles calculations it is possible to obtain PES and couplings which allow to perform reliable quantum dynamical simulations to support control experiments. In this case, the relatively easy form of the pulse shape and the intuitive hypothesis of an optimal pump-probe process helped successful interpretation of the intrinsic dynamics of the pulse. More complicated pulse forms may result in more complex reaction paths. For instance, the mere competition of two channels leading to two different chemical products, e.g. competing ligand fragmentation, may involve subtle reaction paths involving control through conical intersections. Another issue to be taken into account is that even if the dissociation starts in the neutral surface it may finish in the ionic states where also crossings of states are possible. Moreover, our simulations use a zero kinetic energy (ZEKE) approach, meaning that the photodetachment process is not simulated discretizing the continuum but asumming quasiresonant transitions between neutral and ionic states [50]; the account of continuum states or even a time-dependent description of the photodetached electron may uncover important details of the ionization process. Any of the aspects just mentioned constitutes an issue in itself. Hence, the simultaneuos consideration of all such factors by the simulation of close-loop or adaptive control experiments can still pose a considerable challenge for theoreticians.

In any case, the combined efforts of future laser experiments and theoretical simulations will further illuminate the fascinating relationships between light and molecular structures which one day may lead chemists to use crafted laser pulses as new reagents [51].

Acknowledgements The authors gratefully thank Prof. J. Manz as well as Prof. L. Wöste and coworkers for many useful and fruitful discussions. Financial support was provided by the Deutscheforschungsgemeinschaft via the Sonderforschungsbereich 450, “Analysis and control of ultrafast photoinduced reactions”.

References

1. Zewail AH (2000) (Nobel lecture) Angew Chem Int Ed 39:2586
2. Crim F (1990) Science 249:1387
3. Shapiro M, Brumer P (1986) Chem Phys Lett 126:541
4. Tannor DJ, Rice SA (1985) J Chem Phys 83:5013
5. Tannor DJ, Kosloff R, Rice SA (1986) J Chem Phys 85:5805
6. Bergmann K, Theuer H, Shore BW (1998) Rev Mod Phys 70:1003
7. Rabitz H, de Vivie-Riedle R, Motzkus M, Kompa K (2000) Science 288:824
8. Baumert T, Thalweiser R, Weiss V, Gerber G (1995) Femtosecond chemistry, VCH, Weinheim
9. Zhu L, Suto K, Fiss J, Wada R, Seidan T, Gordon RJ (1997) Phys Rev Lett 78:4108
10. Thompson DL (1998) Modern methods for multidimensional dynamics computations in chemistry, World Scientific, Singapore
11. Kühn O, Manz J, Miller WH (eds) (2004) Multidimensional quantum reaction dynamics, vol 304 (1–2), Chem Phys (special issue)
12. Judson RS, Rabitz H (1992) Phys Rev Lett 68:1500
13. Brixner T, Gerber G (2003) Chem Phys Chem 4:418
14. Bardeen CJ, Yakovlev V, Wilson K, Carpenter S, Weber PM, Warren W (1997) Chem Phys Lett 280:151
15. Assion A, Baumert T, Bergt M, Brixner T, Kiefer B, Seyfried V, Strehle M, Gerber G (1998) Science 282:919
16. Brixner T, Damrauer NH, Gerber G, Niklaus P (2001) Nature 414:57
17. Glaß A, Rozgonyi T, Feurer T, Szabó G, Sauerbrey R (2000) Appl Phys B71:267
18. Levis RJ, Menkir GM, Rabitz H (2001) Science 292:709
19. Vajda Š et al (2002) Ultrafast dynamics in molecular science, World Scientific, Singapore
20. Herek JL, Wohlleben W, Cogdell RJ, Zeidler D, Motzkus M (2002) Nature 417:533
21. Geremia JM, Zhu WS, Rabitz H (2000) J Chem Phys 113:10841
22. Hornung T, Motzkus M, de Vivie-Riedle R (2001) J Chem Phys 115:3105–3110
23. Hornung T, Motzkus M, de Vivie-Riedle R (2002) Phys Rev A 65:021403
24. Kurtz L, Rabitz H, de Vivie-Riedle R (2002) Phys Rev A 65:032514
25. Zhu W, Rabitz H (1999) J Chem Phys 111:472
26. Mitra A, Rabitz H (2003) Phys Rev A 67:033407
27. White JL, Pearson BJ, Bucksbaum PH (2004) quant-ph/0401018
28. Mancal T, May V (2002) Chem Phys Lett 362:407
29. Daniel C, Full J, González L, Lupulescu C, Manz J, Merli A, Vajda S, Wöste L (2003) Science 299:536
30. Manz J, Wöste L (eds) (1995) Femtosecond chemistry, VCH, Weinheim
31. Eickeyer F, Kaindl RA, Woerner M, Elsaesser T, Weiner AM (2000) Opt Lett 25:1472
32. Witte T, Hornung T, Windhourn L, Proch D, de Vivie-Riedle R, Motzkus M, Kompa KL (2003) J Chem Phys 118:2021
33. Olivucci M (ed) (2005) Computational photochemistry, Elsevier, Amsterdam
34. Banares L, Baumert T, Bergt M, Kiefer B, Gerber G (1997) Chem Phys Lett 267:141
35. Trushin SA, Fuss W, Schmid WE, Kompa L (1998) J Phys Chem 102:4129
36. Trushin SA, Fuss W, Kompa L, Schmid W (2000) Chem Phys 259:313
37. Matsubara T, Daniel C, Veillard A (1994) Organometallics 13: 4905
38. Daniel C, Kolba E, Lehr L, Manz J, Schröder T (1994) J Phys Chem 98:9823
39. Finger K, Daniel C, Saalfrank P, Schmidt B (1996) J Phys Chem 100:3368
40. Erdman M, Rubner O, Shen Z, Engel V (2001) Chem Phys Lett 341:338
41. Rubner O, Engel V (2001) J Chem Phys 115:2936
42. Paterson MJ, Hunt PA, Robb MA, Takahashi O (2002) J Phys Chem 106:10494
43. Trushin SA, Fuss W, Schmid W (2004) J Chem B 37:3987
44. Full J, Daniel C, González L (2001) J Phys Chem A 105:184
45. Full J, Daniel C, González L (2003) Phys Chem Chem Phys 5:87
46. Daniel C, Full J, González L, Kaposta C, Krenz M, Lupulescu C, Manz J, Minoto S, Oppel M, Rosendo-Francisco P, Vajda Š, Wöste L (2001) Chem Phys 267:247
47. Hirsch G, Bruna PJ, Buenker RJ, Peyerimhoff SD (1980) Chem Phys 45:335
48. Baer M (1975) Chem Phys Lett 35:112
49. Full J, González L, Manz J (2005) Chem Phys 314:143
50. Schön J, Köppel H (1999) J Phys Chem 103:8579
51. Rabitz H (2003) Science 299:525